ACS NANO

www.acsnano.org

ARTICLE

Enhanced Layer-Breathing Modes in van der Waals Heterostructures Based on Twisted Bilayer Graphene

He Hao,[#] Miao-Ling Lin,[#] Bo Xu,[#] Heng Wu, Yuechen Wang, Hailin Peng, Ping-Heng Tan,* Lianming Tong,* and Jin Zhang

Cite This: *ACS Nano* 2023, 17, 10142–10151

Read Online

ACCESS | Metrics & More | Article Recommendations | Supporting Information

ABSTRACT: **The characterization of interlayer coupling in two-dimensional van der Waals heterostructures (vdWHs) is essential to understand their quantum behaviors and structural functionalities. Interlayer shear and layer-breathing (LB) phonons carry rich information on interlayer interaction, but they are usually too weak to be detected via standard Raman spectroscopy due to the weak electron−phonon coupling (EPC). Here, we report a universal strategy to enhance LB modes of vdWHs based on twisted bilayer graphene (tBLG). In both tBLG/hBN and tBLG/MoS_2 vdWHs, the resonantly excited electrons in tBLG can strongly couple to LB phonons extended over the entire layers in the vdWHs, whose resonance condition is tunable by the twist angle of tBLG. In vdWHs containing twisted graphene layers with multiple twisted interfaces, the EPC of LB phonons coming from the collective LB vibrations of entire heterostructure layers can be tuned by resonant excitation of programmable van Hove singularities according to each twisted interface. The universality and tunability of enhanced LB phonons by tBLG make it a promising method to investigate EPC and interlayer interaction in related vdWHs.**

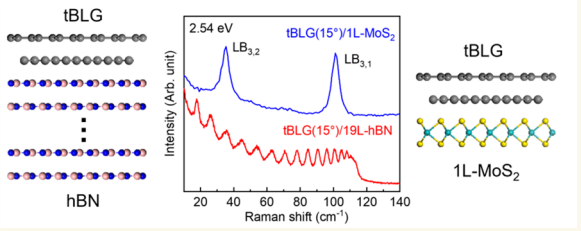

KEYWORDS: *van der Waals heterostructures, layer breathing modes, twisted bilayer graphene, interlayer interaction, electron−phonon coupling, Raman spectroscopy*

INTRODUCTION

van der Waals heterostructures (vdWHs) stacked by different two-dimensional materials (2DMs) present optical,[1,2] electrical,[3,4] and magnetic[5,6] properties that are not accessible in their individual constituents. Among them, graphene-based vdWHs, where graphene layers serve as heterostructure constituent, have been extensively studied due to their quantum behaviors such as the formation of a Hofstadter's butterfly pattern[3,7] and the realization of electron correlated states.[4,8−10] From the viewpoint of practicality, graphene-based vdWHs also widely exist in applications including electronic devices[11,12] and remote epitaxy.[13,14] Owing to the 2D nature of constituent layered materials, interlayer interaction holds the key to fully understanding the exotic properties and optimizing the functionalities of graphene-based vdWHs. For instance, the interlayer contact between graphene electrodes and channel material free of bubble and containment is necessary for high performance;[15,16] and a weak interlayer van der Waals force between the graphene substrate and as-grown material in remote epitaxy is essential for the following exfoliation process.[14] The characterization of interlayer interaction is crucial for further investigation and application of graphene-based vdWHs.

Interlayer phonons involve the relative motion between the adjacent atomic planes, and are natural indicators of interlayer interaction.[17−19] According to the vibration direction, interlayer phonons can be divided into interlayer shear[17] and layer-breathing (LB) modes[18] (i.e., the rigid-layer out-of-plane vibration mode, which can also be called the compression mode[20,21]). For graphene-based vdWHs consisting of constituents with strong coupling strength between interlayer phonons and specific excited electrons or excitons, interlayer phonons of the vdWHs can be conveniently probed by resonance Raman spectroscopy,[22−24] which makes it possible to study the interlayer interaction. For example, LB phonon

Received: January 2, 2023
Accepted: May 30, 2023
Published: June 2, 2023

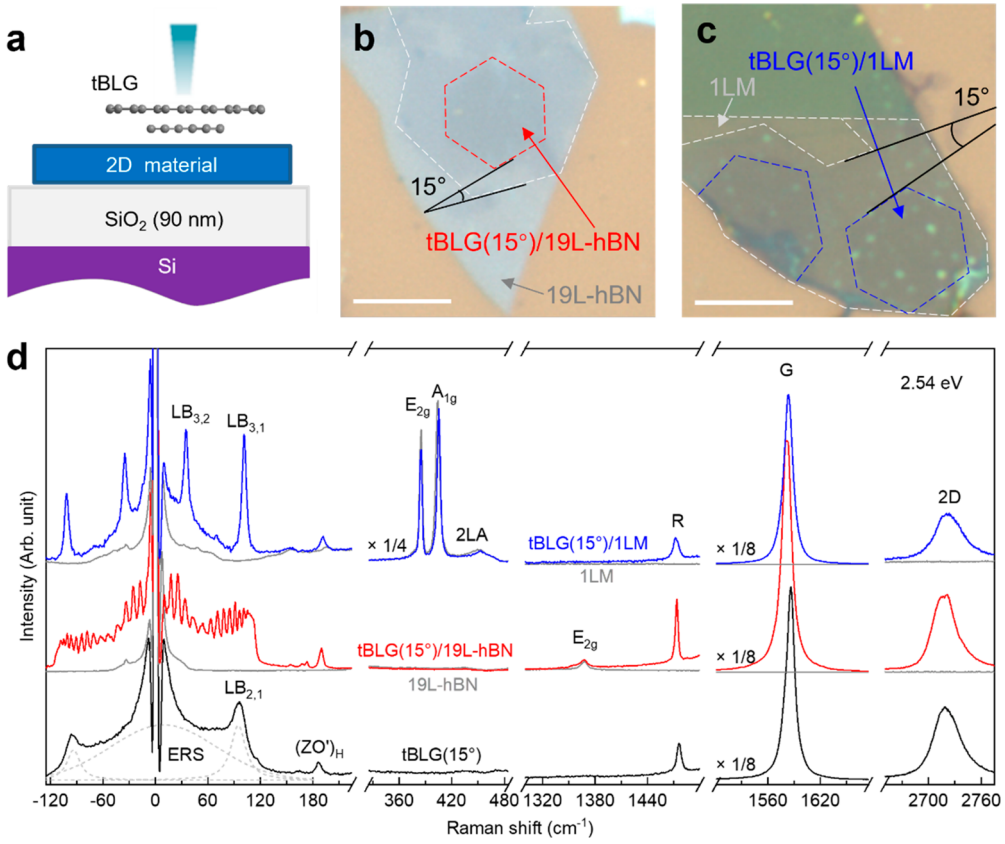

Figure 1. Optical microscope images and Raman spectra of tBLG/2DM vdWHs. (a) Illustration of tBLG/2DM vdWHs. (b,c) Optical microscope images of (b) tBLG(15°)/19L-hBN and (c) tBLG(15°)/1LM. The white dashed lines indicate the SLG/2DM regions; the red and blue dashed hexagons depict the tBLG/2DM regions. The black solid lines show interlayer twist angles between the two SLG layers in tBLG/2DM vdWHs. Scale bar, 5 μm. (d) Raman spectra of tBLG(15°), 19L-hBN, tBLG(15°)/19L-hBN, 1LM, and tBLG(15°)/1LM. Gray dashed lines show the Lorentzian fitting of LB and ERS modes. The spectra are scaled and offset for clarity and the scale factors are shown. "1LM" is the abbreviation for monolayer MoS_2.

modes have been used to measure the interfacial layer-breathing force constant between MoS_2 and graphene.[22,25] Unfortunately, this method is not applicable to vdWHs with small electron−phonon coupling (EPC) strength in each constituent, and there is nearly no report on interlayer Raman modes for other graphene-based vdWHs, besides graphene/TMD vdWHs. Thus, a universal strategy to enhance the interlayer Raman modes in different kinds of graphene-based vdWHs is greatly desired.

Herein, we report the universal enhancement of LB modes in twisted bilayer graphene (tBLG)/2DM vdWHs, where the 2DM can be either insulating hBN, or semiconducting transition metal dichalcogenides (TMDs). Taking advantages of resonant excitation between conduction and valence van Hove singularities (VHSs) in the electronic density of states (DOS) of tBLG,[26,27] LB phonons coming from the collective LB vibrations of entire layers in the vdWHs can strongly couple to resonantly excited electrons related to conduction VHS in tBLG constituent. By tuning interlayer twist angle in tBLG, energy difference between conduction and valence VHSs (ΔE_{VHS}) can be easily modulated to fulfill resonance excitation and realize obvious LB modes enhancement at any laser energy in the visible range. The enhancement mechanism can be well explained by the interlayer bond polarizability model in vdWHs, which precisely captures the spectral features of enhanced LB modes in tBLG/2DM with different constituents and layer numbers. The technique can be further extended to twisted trilayer graphene (tTLG)/2DM vdWHs, where the EPC can be programed to realize enhanced LB modes under multiple excitation energies. Our work provides a universal strategy to study interlayer interaction in graphene-based vdWHs, and showcases the great potential of twisted graphene layers in both fundamental studies and practical applications.

RESULTS AND DISCUSSION

Observation of LB Modes in tBLG/2DM vdWHs. tBLG used in this work was directly grown by chemical vapor deposition (CVD) method, while other 2DMs were prepared by mechanical exfoliation. tBLG/2DM (Figure 1a) vdWHs were fabricated by transferring tBLG on 2DM or vice versa. To evaluate the possible influence of the CVD process, 2DM/tBLG was also prepared by a dry pick-up technique using only mechanical exfoliated single layer graphene (SLG) and 2DM (see Methods). For tBLG with an interlayer twist angle of θ, we name it as tBLG(θ) (see Methods for details about θ determination); and for n-layer hBN and m-layer MoS_2, we abbreviate them as nL-hBN and mLM, respectively. Figure 1 b and c show the optical microscope images of tBLG(15°)/19L-hBN and tBLG(15°)/1LM. The layer numbers of hBN and MoS_2 were identified respectively by atomic force microscope (AFM) (Figure S1) and interlayer Raman modes[18] before transfer. And the layer number of hBN was further confirmed by the LB modes of the corresponding vdWHs. The red and

https://doi.org/10.1021/acsnano.3c00022
ACS Nano 2023, 17, 10142−10151

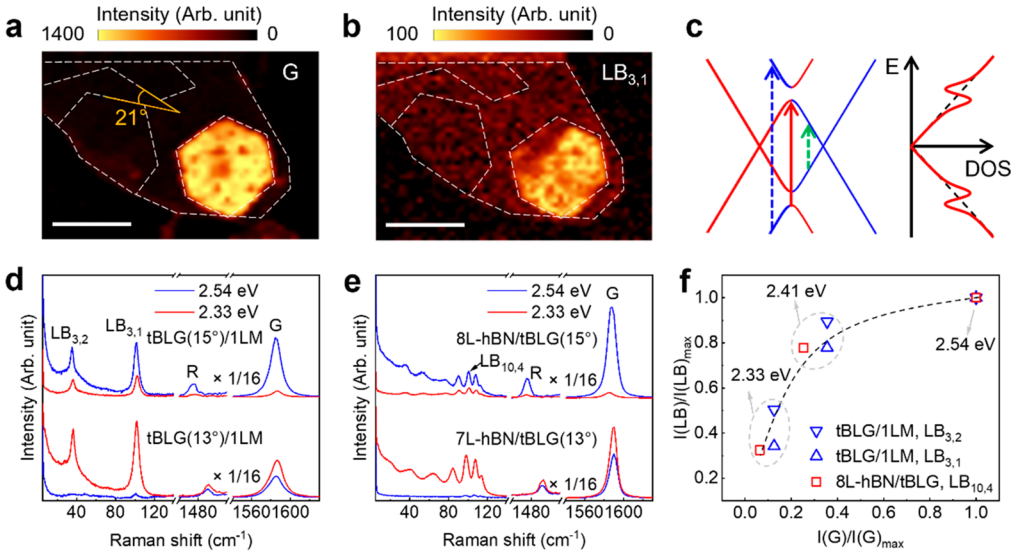

Figure 2. Intensity enhancement of LB modes in tBLG/2DM and 2DM/tBLG vdWHs. (a,b) Raman intensity mapping of (a) G mode and (b) $LB_{3,1}$ mode in tBLG/1LM vdWHs shown in Figure 1c. The excitation energy is 2.54 eV. White dashed lines are guide to eyes indicating different vdWHs regions. The yellow solid lines mark the interlayer twist angle between two SLG layers in tBLG(21°)/1LM. Scale bar, 5 μm. (c) Illustration of local electronic band structures and the corresponding electronic density of states for tBLG with twist angle larger than 10°. The red solid arrow and blue/green dashed arrows represent the resonant and nonresonant optical transitions between conduction and valence VHSs, respectively. (d,e) Raman spectra of different tBLG/2DM and 2DM/tBLG vdWHs under 2.33 eV and 2.54 eV excitations. The spectra are scaled and offset for clarity and the scale factors are shown. The Raman intensity is normalized by the E_1 mode of quartz at ~127 cm^{-1} to eliminate different efficiencies of the charge-coupled device at different excitation energies. (f) Intensity statistics showing relationship between the intensities of LB and G modes in tBLG(15°)/1LM and 8L-hBN/tBLG(15°) vdWHs under 2.33 eV, 2.41 eV, and 2.54 eV excitations. Intensities of different scattering modes are respectively normalized to their maximum intensities under resonant excitation. Data obtained under the same excitation energy are marked in the same gray dashed circle with the excitation energy noted by the side. Black dashed curve is guide to eyes showing positive correlation between the intensities of LB and G modes. The original spectra are presented in Figure S5.

blue dashed hexagons indicate the tBLG/2DM vdWHs regions.

Figure 1d shows Raman spectra of tBLG(15°), 19L-hBN, 1LM, tBLG(15°)/19L-hBN, and tBLG(15°)/1LM. In tBLG(15°), the G mode intensity is significantly enhanced under 2.54 eV excitation, which is due to the resonant excitation between VHSs in the valence and conduction bands.[23,26,28] The high-frequency features above 120 cm^{-1} are simple superpositions of phonon modes from each heterostructure constituent. The peak frequencies of the so-called $(ZO')_H$[29] (from LB phonon branch) and R (from transverse optical phonon branch) modes activated by moiré superlattice in tBLG(15°)/2DM are almost the same as those in tBLG(15°), which suggests that the variation in twist angle between two graphene layers in tBLG is negligible during the transfer process.[27,29,30] Besides, the significant G mode enhancement is still observed in both tBLG(15°)/19L-hBN and tBLG(15°)/1LM, demonstrating that the VHS-related resonance behaviors remained in tBLG/2DM. The above results lay the foundation for investigating the resonance mechanism of the LB modes in tBLG/2DM vdWHs as discussed below.

In the low-frequency region of tBLG(15°), a broad peak is located from ~ −150 cm^{-1} to 150 cm^{-1}, which is consistent with previous reports,[17,29] and is assigned as an electronic Raman scattering (ERS) mode originating from low-energy excitations or inelastic scattering of free carriers.[17] For 19L-hBN, no interlayer phonon mode is observed because the EPC strength of interlayer shear and LB phonons in hBN flakes is extremely weak under visible laser excitation.[24] In 1LM, there is no interlayer interaction and thus no interlayer phonon mode exists in the low-frequency region. However, when tBLG(15°) is placed above 19L-hBN or monolayer MoS_2 to form tBLG/2DM vdWHs, the low-frequency features become strikingly different from those of the individual constituents. In both tBLG(15°)/19L-hBN and tBLG(15°)/1LM, multiple additional LB modes emerge, which is confirmed by polarized Raman measurements[18] (Figure S2, Supporting Information). The detailed discussion one the reason why the rigid shear mode is not observed in tBLG/hBN and hBN/tBLG is presented in Note S1 (Supporting Information). The observation of these LB modes is independent of stacking orders and vdWHs fabrication method (Figure S3). Similar results can also be observed in other tBLG(15°)/2DM vdWHs such as tBLG(15°)/1L-WS_2 and tBLG(15°)/1L-ReS_2 (Figure S4), which demonstrates the universality of this unusual phenomenon. These LB modes come from the collective LB vibrations of entire layers in the vdWHs,[24] which will be discussed in detail in what follows.

It is worth noting that the twisted stacking between different vdWH constituents may lead to the formation of moiré patterns depending on twist angle φ, which will modify interlayer LB coupling.[19] According to previous report on MoS_2/graphene vdWHs, φ has little influence on LB modes, because the mismatch of the in-plane lattice constant between MoS_2 and graphene is too large to form moiré patterns.[22] However, the in-plane lattice constant between hBN and graphene is only about ~1.8%,[31] thus the influence of moiré patterns formed at the hBN/graphene interface is not negligible. To simplify the analysis in this work, we identified

https://doi.org/10.1021/acsnano.3c00022
ACS Nano 2023, 17, 10142−10151

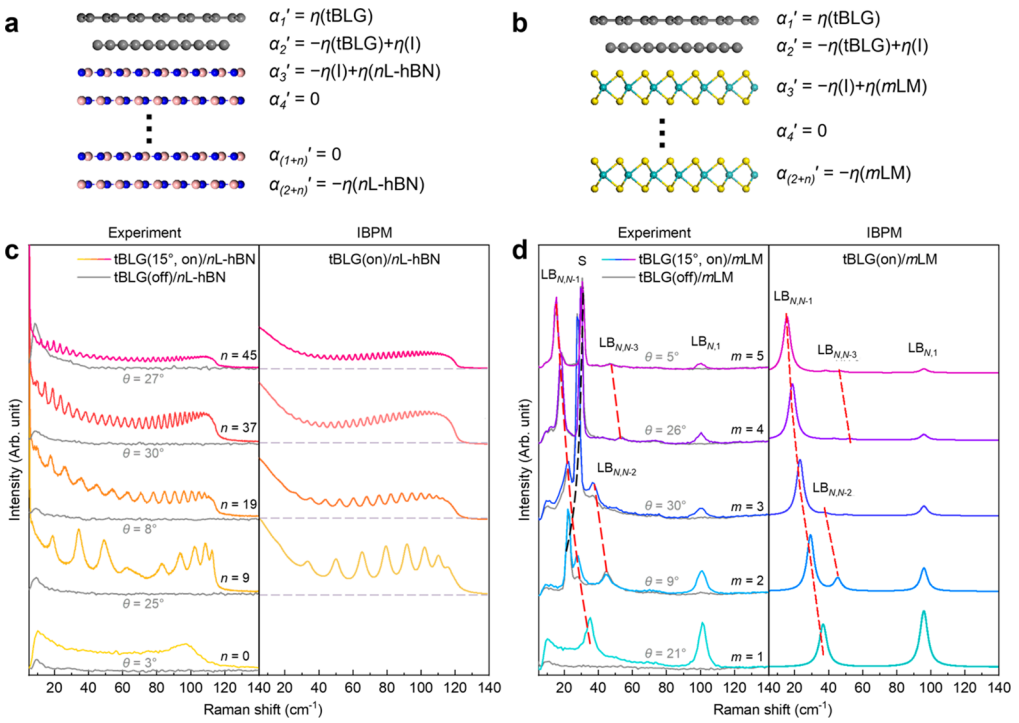

Figure 3. Intensity enhancement mechanism of the LB modes elaborated by interlayer bond polarizability model. (a,b) Schematic diagram explaining the interlayer bond polarizability model of LB modes in (a) tBLG/*n*L-hBN and (b) tBLG/*m*LM. (c,d) Raman spectra of (c) tBLG/*n*L-hBN and (d) tBLG/*m*LM with different values of *n* and *m*. tBLG(15°, on)/2DM indicates that tBLG with $\theta \sim 15°$ in vdWHs is on-resonant under 2.54 eV excitation. tBLG(off)/2DM indicates that tBLG with θ smaller than 10° or larger than 20° in vdWHs is off-resonant under 2.54 eV excitation. The values of θ for each tBLG(off)/2DM vdWHs are shown beside the corresponding spectrum. Red (black) dashed lines in (d) are guide to eyes showing the evolution of LB modes (shear modes).

the crystal orientation of the adjacent hBN and graphene layers using the crystalline edges (Figure S1), and intentionally controlled φ to be larger than 7° to minimize the LB coupling modification from moiré patterns.[19] Low-frequency Raman signatures of tBLG/hBN and hBN/tBLG vdWHs with $\varphi < 7°$ will be discussed elsewhere.

Resonance Behavior of LB Modes Enhanced by tBLG. Figures 2a,b present the Raman intensity mapping of 2.54 eV-excited G and $LB_{3,1}$ modes (see Methods for the detailed denotations of LB modes) of tBLG/1LM shown in Figure 1c. The resonance enhancement of the G mode is only observed in tBLG(15°)/1LM, in striking contrast to the adjacent tBLG(21°)/1LM region. As indicated in Figure 2c, the excitation energy of 2.54 eV matches the energy difference between conduction and valence VHSs in a 15° tBLG (red arrow in Figure 2c). While for tBLG(21°), larger twist angle leads to greater energy separation between conduction and valence VHSs,[26] and therefore the excitation energy of 2.54 eV is too small to satisfy the resonant excitation. Interestingly, as shown in the Raman intensity mapping of the $LB_{3,1}$ mode in Figure 2b, the $LB_{3,1}$ mode observed in tBLG/1LM shows similar resonance behavior to the G mode, which is only enhanced in tBLG(15°)/1LM region (the representative spectra of tBLG(15°)/1LM and tBLG(21°)/1LM can be found at the bottom of "Experiment" column of Figure 3d in cyan and gray colors, respectively).

To further investigate the resonance mechanism of the LB modes in tBLG/2DM and 2DM/tBLG, we fabricated tBLG/1LM and hBN/tBLG with different twist angles in the tBLG constituent, and measured the Raman spectra with multiple excitation energies. The corresponding results are presented in Figure 2d,e, Figures S5 and S6. As shown in Figure 2d,e, the twist angle θ of tBLG can be confirmed by the R mode frequency, which blue shifts with decreasing twist angle.[27,30] The determination of θ is further verified in Figure S7 according to the θ-dependence of out-of-plane acoustic (ZA, $(ZO')_H$), longitudinal acoustic (LA), and out-of-plane transverse optical (oTO) mode frequencies based on theoretical approximations for the phonon dispersion relations in graphene.[32,33] tBLG exhibits smaller energy separation between conduction and valence VHSs[26,28] with the decrease of its twist angle, so that the resonant excitation energy for tBLG(13°) is about 2.33 eV, while that of tBLG(15°) is close to 2.54 eV. Under different resonance conditions, LB modes in different vdWHs show a similar resonance behavior, whose intensities are in positive correlation with the G mode intensity (Figure 2f and Figure S5). In other words, the resonance mechanism of the LB modes in tBLG/2DM and 2DM/tBLG is dictated by the VHS-related optical transition of the tBLG constituent in the heterostructures. More detailed discussion about the resonance mechanism for LB modes is presented in Note S2. The above results validate that tBLG can be used as a special constituent to universally enhance the LB modes coming from the collective vibrations of the entire layers in the vdWHs.

Mechanism of LB Modes Enhancement via tBLG. The enhanced LB modes in tBLG-based vdWHs via the resonant excitation corresponding to the VHS-related optical transition energy in tBLG constituent suggest strong constituent-vdWH electron−phonon coupling of LB phonons in tBLG/2DM vdWHs, which can be mediated by strong interfacial coupling between tBLG and 2DM constituents.[24] Qualitatively, the

https://doi.org/10.1021/acsnano.3c00022
ACS Nano 2023, 17, 10142−10151

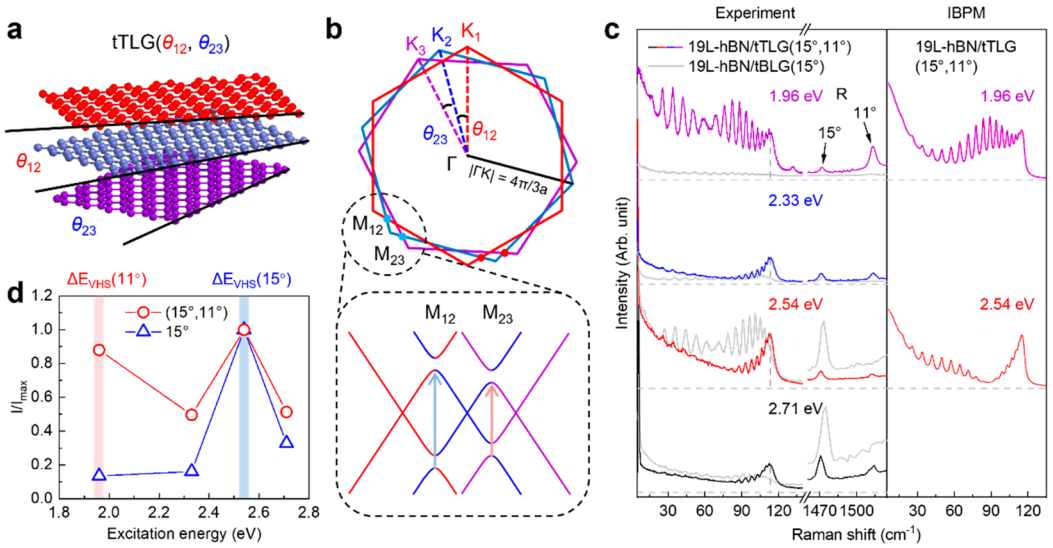

Figure 4. Designable resonance behavior of LB modes in hBN/tTLG. (a) Schematics of tTLG(θ_{12}, θ_{23}). θ_{12} and θ_{23} are interlayer twist angles between top/middle and middle/bottom SLG layers. $\theta_{12} + \theta_{23} < 30°$. (b) Brillouin zone and local electronic band structures of tTLG(θ_{12}, θ_{23}). The red, blue, and purple hexagons are the first Brillouin zones of top, middle, and bottom SLG layers, respectively. Equivalent K points of different layers are indicated as K_1, K_2, and K_3 with same colors as the corresponding first Brillouin zones. VHSs resulting from θ_{12} and θ_{23} are located at M_{12} and M_{23}. a = 0.246 nm is the lattice constant of SLG. (c) Raman spectra of 19L-hBN/tTLG(15°, 11°) and 19L-hBN/tBLG(15°) under 1.96 eV, 2.33 eV, 2.54 eV, and 2.71 eV excitations. R modes originating from twisted stacking between different adjacent SLG layers are shown with corresponding interlayer twist angles. The vertical gray dashed lines indicate the spectral height at 112.5 cm^{-1}. The Raman intensity is normalized by the E_1 mode of quartz at ~127 cm^{-1} to eliminate different efficiencies of a charge-coupled device at different excitation energies. The right panel shows the calculated Raman spectra of 19L-hBN/tTLG(15°, 11°) under 1.96 eV and 2.54 eV excitations by the IBPM of vdWHs. (d) Resonance profiles of LB modes for 19L-hBN/tTLG(15°, 11°) and 19L-hBN/tBLG(15°). The spectral height at 112.5 cm^{-1} is taken as the indicator of LB modes intensities, which is normalized to the maximum intensity obtained under 2.54 eV excitation.

mechanism of the LB mode enhancement can be explained based on the theory of constituent-vdWH EPC:[24] First, the excitation photons with the energy of ΔE_{VHS} can be strongly absorbed by the tBLG constituent in tBLG/2DM and 2DM/tBLG to generate the resonantly excited electrons and holes in the tBLG constituent. Then, these excited electrons and holes can strongly couple with the LB vibration within tBLG constituent.[23] Due to the strong interfacial LB coupling between 2DM and tBLG constituents, there will be strong interaction between the LB vibration in tBLG and those in the 2DM constituent, which leads to the collective LB vibrations of entire layers in the vdWHs,[24] as observed in our experiment. For a quantitative analysis, we first examine the interfacial coupling between tBLG and nL-hBN (or mLM). Two typical schematics of tBLG/nL-hBN and tBLG/mLM vdWHs are shown in Figure 3a,b. We measured the Raman spectra of LB phonons in tBLG/nL-hBN and tBLG/mLM vdWHs with varied layer numbers of MoS_2 and hBN constituents (Figure 3c,d), in which the peak positions of the observed LB modes (Pos(LB)) for both vdWHs are sensitive to the layer numbers of the hBN and MoS_2 constituents. With increasing the number of layers, more LB modes emerge. By fitting the Pos(LB) in vdWHs by the linear chain model (LCM) with the reported LB coupling force constants of tBLG[23] ($\alpha^{\perp}$(tBLG) = 10.6 × 10^{19} N·m^{-3}), hBN[24] ($\alpha^{\perp}$(nL-hBN) = 9.88 × 10^{19} N·m^{-3}), and MoS_2[22,25,34] ($\alpha^{\perp}$(mLM) = 8.65 × 10^{19} N·m^{-3}), we can yield the interfacial coupling between tBLG and nL-hBN ($\alpha^{\perp}$(tBLG/nL-hBN)) or mLM ($\alpha^{\perp}$(tBLG/mLM)) constituents, i.e., $\alpha^{\perp}$(tBLG/nL-hBN) = 9.9 × 10^{19} N·m^{-3}, $\alpha^{\perp}$(tBLG/mLM) = 5.7 × 10^{19} N·m^{-3}, in good agreement with the previous study.[25] Based on the LCM, we also plot the normal mode displacements for each LB mode observed in tBLG(15°)/1LM and 7L-hBN/tBLG(13°) in Figure S10 to better describe the vibration origin of each LB mode, from which we can find that the LB phonons are from the collective vibrations of the entire layers in the vdWHs. The fitted interfacial LB coupling force constants are comparable to those within tBLG, which efficiently bridges the coupling between the resonantly excited electrons in tBLG constituent and LB phonons extended over the entire tBLG-based heterostructures.

Figure 3 c and d reveal a significant difference of the relative Raman intensity of the observed LB modes between tBLG/nL-hBN and tBLG/mLM vdWHs. More specifically, tBLG/mLM vdWHs possess enhanced $LB_{N,N-1}$ modes (N is the total layer number of vdWHs), while the LB modes in tBLG/nL-hBN vdWHs show more uniformly distributed Raman intensity in a wide spectral range. To further quantify such constituent-vdWH EPC in tBLG-based vdWHs, we extend the interlayer bond polarizability model (IBPM) of vdWHs[24] to understand the relative Raman intensity of LB modes in vdWHs. In the IBPM, the Stokes Raman intensity is proportional to the square of the change of vdWH's polarizability ($\Delta\alpha$), i.e., $I \propto \frac{1+n_j}{\omega_j}|\Delta\alpha|^2$, in which n_j and ω_j are, respectively, Bose–Einstein population factor and peak position of $LB_{N,N-j}$, and $\Delta\alpha$ can be expressed by the polarizability change of each layer, $\Delta\alpha = \sum_i \alpha_i' \cdot u_j^i$. α_i' is the polarizability derivative of i^{th} layer with respect to the interlayer displacements (u_j^i) of the $LB_{N,N-j}$ mode. As reported,[24,35] only the layers with one neighboring layer or two nonequivalent neighboring layers have nonzero α_i', e.g. $\alpha'_1 = \eta$(tBLG), $\alpha'_2 = -\eta$(tBLG)+η(I), as demonstrated in Figure 3a,b. Here, η(X) (X = tBLG, nL-hBN, and mLM)

https://doi.org/10.1021/acsnano.3c00022
ACS Nano 2023, 17, 10142–10151

represents a fitting parameter related to the properties of the interlayer bond, such as interlayer bond length and polarizabilities, in the tBLG, nL-hBN, and mLM constituents, η(I) represents a fitting parameter related to the interface (I) between tBLG and nL-hBN (or mLM). η(X) and η(I) are sensitive to the laser energy. η(tBLG) reaches a maximum when the laser energy matches the energy separation between conduction and valence VHSs, while η(mLM) reaches a maximum when the laser energy is resonant with the C exciton energy of mLM.[24] Under visible laser excitation, η(nL-hBN) is usually negligible as the excitation energy is always below the bandgap of insulator hBN. For tBLG/nL-hBN vdWHs, the Raman intensity profiles of the LB modes can be well fitted by η(tBLG) = 1, η(I) = 0.05, η(nL-hBN) = 0, and the corresponding calculated results are shown in the right panel of Figure 3c. This exactly confirms that the LB modes are resonantly enhanced when the excitation energy matches the energy difference between conduction and valence VHSs of tBLG constituent in tBLG/nL-hBN vdWHs. Notably, to reproduce the measured Raman spectra of LB modes in tBLG/nL-hBN vdWHs, a Lorentzian peak with central peak position of 0 cm^{-1} and full width at half-maximum of 40 cm^{-1} is used to fit the ERS. On the other hand, under 2.54 eV excitation, tBLG(15°) and mLM constituents of tBLG/mLM vdWHs are both resonantly excited, as 2.54 eV is close to optical transition between conduction and valence VHSs of tBLG constituent and the C exciton of mLM constituent. Thus, the coupling of LB phonons in tBLG/mLM vdWHs to the excited electrons in tBLG and C excitons in mLM accounts for the Raman intensity of the LB modes. Indeed, when η(mLM) = η(tBLG) = 1 and η(I) = 0.2, the calculated Raman spectra by the IBPM are in good agreement with the experimental ones, as illustrated in Figure 3d. Therefore, the enhancement of the $LB_{N,N-1}$ modes in tBLG/mLM originates from the strong constituent-vdWH EPC of LB phonons to electrons/excitons in tBLG and mLM constituents. These results suggest the possibility to modulate Raman intensity of LB modes in vdWHs via various resonance conditions of the corresponding constituents.

Manipulating Resonance Behaviors of LB Modes via Twisted Trilayer Graphene. Considering that the formation of VHSs only requires twisted stacking of two adjacent single graphene layers, one can expand the enhancement of LB modes to more complicated vdWHs based on twisted graphene layers consisting of more than one twisted interface. In the twisted multilayer graphene constituent, each interlayer twist angle can serve as an independent degree of freedom to generate VHSs with corresponding energy separation, which makes it possible to achieve enhanced LB modes under multiple excitations. For instance, twisted trilayer graphene (tTLG) has two twisted vdW interfaces with corresponding interlayer twisted angles θ_{12} and θ_{23} (Figure 4a). If the bottom SLG rotates clockwise relative to the top SLG at each twisted interface, they will form two set of VHSs at M_{12} and M_{23} in momentum space (Figure 4b). According to the enhancement mechanism discussed above, resonant excitation between either set of VHSs can lead to the enhancement of LB mode intensity. To test this hypothesis, we fabricated 19L-hBN/tTLG(15°, 11°) and 19L-hBN/tBLG(15°) heterostructures. For 19L-hBN/tTLG(15°, 11°), there are two R modes located at 1472 and 1513 cm^{-1}, indicating the existence of 15°- and 11°-twisted interfaces in the tTLG constituent (Figure 4c). To quantify the intensity evolution of LB modes, simultaneous spectra fitting of each LB Raman peak and ERS background is necessary. However, it is hard to determine the exact line shape of the broad ERS background underneath multiple Raman signals of LB modes, which hinders the correct extraction of LB mode intensities. As a compromise, we finally take spectral height at 112.5 cm^{-1} (vertical gray dashed lines in Figure 4c) as an indicator of the resonance status of the LB modes. 19L-hBN/tTLG(15°, 11°) shows a local intensity maximum at 112.5 cm^{-1}, where the ERS intensity is expected to be negligible according to the spectra fitting of tBLG(15°) (Figure 1d). Therefore, the variation of spectral height at 112.5 cm^{-1} is mainly governed by different resonance responses of the LB modes. As shown in the quantitative analysis of Figure 4d, 19L-hBN/tTLG(15°, 11°) shows clear resonance enhancement under both 1.96 eV and 2.54 eV excitations, which respectively corresponds to the energy separation between conduction and valence VHSs of 11°- and 15°-twisted interfaces in the tTLG constituent (Figure 4b,d). As a comparison, the LB mode intensities in 19L-hBN/tBLG(15°) are only enhanced under a resonant excitation of 2.54 eV. The above results demonstrate that it is possible to program the resonance profiles of LB modes in vdWHs with multiple graphene layers by manipulating the twist angle of each twisted graphene interface.

Interestingly, the low-frequency spectral features of 19L-hBN/tTLG(15°, 11°) are different under 1.96 eV and 2.54 eV resonant excitations. The varied Raman intensity profiles of the LB modes of 19L-hBN/tTLG(15°, 11°) indicate varied strengths of electron−phonon coupling for LB phonons under different resonant excitations related to the two twisted interfaces in the tTLG constituent. We further understand this interesting phenomenon by the interlayer bond polarizability model of vdWHs discussed above. Two fitting parameters η_1(tBLG) and η_2(tBLG) respectively related to the interlayer bond properties at the two twisted interfaces of 15° and 11° should be separately considered under different resonant excitations. Under 2.54 eV excitation, η_1(tBLG) = 1, η_2(tBLG) = 0, while η_1(tBLG) = 0, η_2(tBLG) = 1 for 1.96 eV excitation. The corresponding calculated Raman intensity profiles of the LB modes of 19L-hBN/tTLG(15°, 11°) under 1.96 and 2.54 eV excitations are depicted in the right panel of Figure 4c, which successfully captures the essential experimental observations.

CONCLUSION

In conclusion, we report a universal technique to enhance LB modes in different 2DM/tBLG vdWHs based on twisted graphene layers with designable resonance conditions. The universality and tunability make it suitable to investigate interlayer interaction related properties of vdWHs. Furthermore, from the point of view of electron−phonon coupling, the mechanism features a "nonlocal" form of electron−phonon interaction, where electrons localized within the tBLG constituent or excitons within the semiconductor constituent couple to the delocalized LB phonons from all the stacking layers of vdWHs. This mismatch of spatial distributions of electron and phonon may provide an additional degree of freedom to manipulate EPC to achieve quantum effects as demonstrated by 2DM/tTLG in this work. Finally, using tBLG to study moiré-related physics based on graphene/hBN superlattices formed at small φ (the twist angle of graphene/hBN interface) is also an uninvestigated but promising direction to explore, where phonon renormalization[19] may

https://doi.org/10.1021/acsnano.3c00022
ACS Nano 2023, 17, 10142−10151

be observed. Considering all of these advantages and opportunities, we believe that twisted graphene layers constitute a promising substrate in future studies to unveil useful information at the vdW interface and manipulate unconventional particle-quasiparticle interactions in 2D heterostructures.

METHODS

Preparation and Characterization of 2DM. The MoS_2, WS_2, ReS_2, and hBN crystals were purchased from HQ Graphene (Netherlands). Polypropylene carbonate (PPC, Mn = 50,000 g mol^{-1}) and benzaldehyde were purchased from Sigma-Aldrich (Shanghai, China). Polydimethylsiloxane (PDMS) was purchased from Gel-Pak (Hayward, CA, USA). The MoS_2, WS_2, ReS_2, and hBN flakes were first deposited on 90 nm SiO_2/Si substrates by the mechanical exfoliation method. The number of layers (or thickness) of hBN flakes was measured by atomic force microscope (AFM) and then confirmed by the interlayer modes of hBN-based vdWHs. The numbers of layers of MoS_2, WS_2, and ReS_2 flakes were directly identified by the interlayer Raman modes.[18]

Preparation of CVD-Grown tBLG. High-quality tBLG samples were grown via a CVD method. During the CVD process, gas-flow perturbation and a heterosite nucleation strategy were employed to increase the fraction of tBLGs in bilayer graphene domains.[36] A piece of Cu foil (50 μm thick, Kunshan Luzhifa Electron Technology Co., Ltd.) was placed in a homemade CVD system that was equipped with a 3-in. quartz tube and was sequentially heated to 800 °C (400 sccm Ar, 30 min), annealed (400 sccm Ar, 10 min), heated to 1020 °C (400 sccm H_2, 10 min), and annealed (400 sccm H_2, 30 min). Subsequently, graphene growth proceeded by introducing CH_4, and the tBLG domain was initiated by increasing the flow rates of H_2 (from 400 to 1000 sccm) and CH_4 (from 0.4 to 1 sccm). After 20 min of growth, the Cu foil was cooled by removing the sample away from the hot zone of the furnace. The tBLG/Cu sample was then spin-coated with PPC in benzaldehyde (0.15 g/mL) at 2500 rpm (45 s) and baked at 80 °C (1 min), followed by the removal of the Cu foil by etching in 1 M $Na_2S_2O_8$ solution. After being washed with deionized water, the PPC/tBLG was placed onto a 90 nm SiO_2/Si substrate.

Determination of Twist Angle between tBLG. Twist angle of tBLG in this work was determined by a combination of different optical characterization methods. For CVD-grown single-crystalline tBLG, the twist angle θ can be first determined by the sharp edges of the top and bottom hexagonal SLG domains (Figure 1b,c and Figure 2a).[36] If 10° < θ < 15°, optical contrast spectra were used to characterize the energy separation between conduction and valence VHSs (ΔE_{VHS}),[28] which can be used to calculate θ by the following relationship: $\theta = 3a\Delta E_{VHS}/4\pi\hbar v_f$, where a = 0.246 nm is the lattice constant of SLG, $\hbar$ is the reduced Planck's constant, and $v_f = 10^6$ m/s is the Fermi velocity in SLG.[26] Then, Raman measurement was performed to further confirm θ by the frequencies of ZA, $(ZO')_H$, LA, oTO, and R modes[27,29,30,32,33] (Figure S7) as well as the resonant behavior of LB_{21} and G modes.[26,29] If θ < 5° or 20° < θ, $(ZO')_H$, R and R′ modes cannot be observed under excitation energies used in this work. In this case, the intensity of the 2D mode is used to determine the approximate value of θ due to the fact that 2D intensity monotonously increases with increasing θ.[26]

Preparation of tBLG/2DM vdWHs Using CVD-Grown tBLG. After determining the twist angle of tBLG, a PDMS film with thickness of 1−2 mm is covered on PPC/tBLG to form the PDMS/PPC/tBLG hybrid structure. The PDMS/PPC/tBLG film was detached from the 90 nm SiO_2/Si substrate with the aid of a water droplet. After that, the PDMS/PPC/tBLG film was stacked on top of 2DM flakes by using a micromanipulator under an optical microscope to form the PDMS/PPC/tBLG/2DM hybrid structure. The PDMS film was easily peeled off from the PPC/tBLG/2DM hybrid structure heated on a hot plate at 110 °C. Subsequently, the PPC film on top of tBLG/2DM was completely removed by washing in acetone at 50 °C, leaving tBLG/2DM on the 90 nm SiO_2/Si substrate.

Preparation of 2DM/tBLG vdWHs Using CVD-Grown tBLG. After determining the twist angle of tBLG, PPC of PPC/tBLG was dissolved in acetone at 50 °C, leaving only tBLG on the SiO_2/Si substrate. A drop of PPC in benzaldehyde (0.15 g/mL) was spin-coated on mechanically exfoliated 2DM flakes on 90 nm SiO_2/Si substrate at 2500 rpm (45 s), followed by covering a PDMS film with a thickness of 1−2 mm to form the PDMS/PPC/2DM hybrid structure. The PDMS/PPC/2DM film was detached from the 90 nm SiO_2/Si substrate with the aid of a water droplet. After that, the PDMS/PPC/2DM film was stacked on top of tBLG flakes by using a micromanipulator under an optical microscope to form the PDMS/PPC/2DM/tBLG hybrid structure. The PDMS film was easily peeled off from the PPC/2DM/tBLG hybrid structure heated on a hot plate at 110 °C. Subsequently, the PPC film on top of 2DM/tBLG was completely removed by washing in acetone at 50 °C, leaving 2DM/tBLG on the 90 nm SiO_2/Si substrate.

Preparation of hBN/tBLG, hBN/tTLG, and 1LM/tBLG vdWHs Using Mechanically Exfoliated SLG, hBN, and 1LM. The graphene flakes (HQ Graphene (Netherlands)) were first deposited on 90 nm SiO_2/Si substrates by the mechanical exfoliation method. The number of layers of graphene flakes can be identified by reflectance contrast spectra and the line shape of Raman 2D mode.[37] hBN/tBLG was fabricated using a dry pick-up technique. A PDMS/PPC/hBN film was prepared by similar procedures mentioned in the previous section, and was then used to tear a SLG flake. The separated graphene pieces were rotated manually by an angle θ and stacked together again, resulting in hBN/tBLG vdWHs. hBN/tTLG and 1LM/tBLG were prepared by a similar method. It is worth noting that tearing SLG with 1LM is more difficult than with hBN, which leads to smaller vdWHs area, poorer interfacial interaction, and weaker LB mode intensity in 1LM/tBLG compared to tBLG/1LM prepared by CVD-tBLG (Figure S3). Therefore, only tBLG/mLM is used in the rest of the paper. In order to enhance the interfacial interaction, all of the vdWHs in this paper were annealed at 300 °C in Ar atmosphere for 30 min before Raman measurements.

Raman Measurements. Raman spectra were measured at room temperature using either a Jobin-Yvon HR-Evolution micro-Raman system or a WITec alpha 300RSA confocal system, both of which are equipped with a liquid-nitrogen-cooled charge couple detector (CCD) and a ×100 objective lens (numerical aperture = 0.90). For the Jobin-Yvon HR-Evolution micro-Raman system, the excitation energies are 1.96 eV, 2.33 eV, 2.41 eV, and 2.54 eV from Ar^+ laser. The 3600, 2400, and 600 lines per mm gratings are used in the Raman measurements. The 3600 lines per mm grating enables each CCD pixel to cover 0.07 cm^{-1} at 2.54 eV. Plasma lines are removed from the laser lines via BragGrate bandpass filters, and the Raman measurements down to 5 cm^{-1} for each excitation are enabled using three BragGrate notch filters with optical density of 3−4 and with full width at half-maximum of 5−10 cm^{-1}. For the WITec alpha 300RSA confocal system, the excitation energies are 2.54 eV with 2400 and 600 lines per mm gratings. The laser power is kept below 0.5 mW to avoid damage to samples.

Linear Chain Model. For the in-plane isotropic 2DMs and the related vdWHs with total number of layers of N, there are N-1 LB modes, denoted as $LB_{N,N-j}$ mode. $LB_{N,1}$ mode corresponds to the highest-frequency LB mode.[17,18] In the linear chain model, each rigid layer of the vdWHs is considered as a ball with layer-breathing force constant interaction ($\alpha^{\perp}$(X), X = tBLG, nL-hBN, mLM, tBLG/nL-hBN, tBLG/mLM), where $\alpha^{\perp}$(tBLG/nL-hBN) and $\alpha^{\perp}$(tBLG/mLM) are the interfacial LB coupling force constants between tBLG and nL-hBN, and between tBLG and mLM constituents, respectively. For hBN/tTLG vdWHs, the second-nearest-neighbor layer-breathing interaction in tTLG ($\beta^{\perp}$(tTLG)) should be considered.[23] The frequency (in cm^{-1}) of the LB modes in tBLG/tTLG-based vdWHs can be calculated by solving an $N \times N$ linear homogeneous equation, $\omega_j^2 M\boldsymbol{u_j} = \frac{1}{4\pi^2c^2}\boldsymbol{D}\boldsymbol{u_j}$, where $\boldsymbol{u_i}$ is the interlayer displacements of $LB_{N,N-j}$ mode with frequency of ω_j, M is the diagonal mass matrix of the vdWH, $c = 3 \times 10^{10}$ cm/s and $\boldsymbol{D}$ is the LB force constant matrix. With the reported LB coupling force constants of tBLG[23] ($\alpha^{\perp}$(tBLG) =

https://doi.org/10.1021/acsnano.3c00022
ACS Nano 2023, 17, 10142−10151

10.6×10^{19} N·m^{-3}), hBN[24] ($\alpha^{\perp}$(nL-hBN) = 9.88×10^{19} N·m^{-3}) and MoS_2[22,25,34] ($\alpha^{\perp}$(mLM) = 8.65×10^{19} N·m^{-3}), we can yield $\alpha^{\perp}$(tBLG/nL-hBN) = 9.9×10^{19} N·m^{-3}, $\alpha^{\perp}$(tBLG/mLM) = 5.7×10^{19} N·m^{-3}, and $\beta^{\perp}$(tTLG) = 0.96×10^{19} N·m^{-3} by fitting the frequencies of the observed $LB_{N,N-j}$ modes in tBLG- and tTLG-based vdWHs. The corresponding interlayer displacements u_j^i at the i^{th} layer along the c axis can be calculated, as exemplified by LB phonons of tBLG(15°)/1LM (top) and 7L-hBN/tBLG(13°) in Figure S10. Therefore, the electron−phonon coupling strength and thus the Raman intensity of the $LB_{N,N-j}$ modes can be obtained by the IBPM of vdWHs, as demonstrated in the main text.

ASSOCIATED CONTENT

Supporting Information

The Supporting Information is available free of charge at https://pubs.acs.org/doi/10.1021/acsnano.3c00022.

Note S1, discussion about why the rigid shear modes are not present in the spectra of tBLG/hBN and hBN/tBLG; Note S2, discussion about other possible resonance mechanisms for LB modes in tBLG/2DM and 2DM/tBLG; Figure S1−S10, AFM image of 19L-hBN flake with thickness of 7.3 nm; the polarized (VV) and depolarized (HV) Raman spectra of tBLG/mLM and tBLG/nL-hBN vdWHs; Raman spectra of tBLG(15°)/2DM and 2DM/tBLG(15°) vdWHs; Raman spectra of tBLG(15°)/1L-MoS_2, tBLG(15°)/1L-WS_2 and tBLG(15°)/1L-ReS_2 vdWHs; Raman spectra of tBLG(15°)/1LM, 8L-hBN/tBLG(15°) and 19L-hBN/tBLG(15°) under excitation energies of 1.96 eV, 2.33 eV, 2.41 and 2.54 eV; Raman spectra of tBLG(13°)/1LM, tBLG(15°)/1LM, tBLG(21°)/1LM, tBLG(16°)/21L-hBN and tBLG(15°)/21L-hBN under excitation energy of 2.54 eV; determination of θ for tBLG(θ), 2DM/tBLG(θ) and tBLG(θ)/2DM vdWHSs using frequencies of ZA, $(ZO')_H$, LA, oTO, and R modes; energy versus momentum diagram and density of electronic states (DOS) for tBLG showing interlayer and intralayer electron−phonon resonance processes; energy versus momentum diagram and DOS for tBLG showing VHS resonance and non-VHS resonance processes; normal mode displacements for each LB modes observed in tBLG(15°)/1LM and 7L-hBN/tBLG(13°) (PDF)

AUTHOR INFORMATION

Corresponding Authors

Ping-Heng Tan − *State Key Laboratory of Superlattices and Microstructures, Institute of Semiconductors, Chinese Academy of Sciences, 100083 Beijing, China;* orcid.org/0000-0001-6575-1516; Email: phtan@semi.ac.cn

Lianming Tong − *Center for Nanochemistry, Beijing Science and Engineering Center for Nanocarbons, Beijing National Laboratory for Molecular Sciences, College of Chemistry and Molecular Engineering, Peking University, 100871 Beijing, China;* orcid.org/0000-0001-7771-4077; Email: tonglm@pku.edu.cn

Authors

He Hao − *Center for Nanochemistry, Beijing Science and Engineering Center for Nanocarbons, Beijing National Laboratory for Molecular Sciences, College of Chemistry and Molecular Engineering, Peking University, 100871 Beijing, China*

Miao-Ling Lin − *State Key Laboratory of Superlattices and Microstructures, Institute of Semiconductors, Chinese Academy of Sciences, 100083 Beijing, China;* orcid.org/0000-0001-5838-8237

Bo Xu − *Center for Nanochemistry, Beijing Science and Engineering Center for Nanocarbons, Beijing National Laboratory for Molecular Sciences, College of Chemistry and Molecular Engineering and Academy for Advanced Interdisciplinary Studies, Peking University, 100871 Beijing, China*

Heng Wu − *State Key Laboratory of Superlattices and Microstructures, Institute of Semiconductors, Chinese Academy of Sciences, 100083 Beijing, China*

Yuechen Wang − *Center for Nanochemistry, Beijing Science and Engineering Center for Nanocarbons, Beijing National Laboratory for Molecular Sciences, College of Chemistry and Molecular Engineering and Academy for Advanced Interdisciplinary Studies, Peking University, 100871 Beijing, China*

Hailin Peng − *Center for Nanochemistry, Beijing Science and Engineering Center for Nanocarbons, Beijing National Laboratory for Molecular Sciences, College of Chemistry and Molecular Engineering, Peking University, 100871 Beijing, China;* orcid.org/0000-0003-1569-0238

Jin Zhang − *Center for Nanochemistry, Beijing Science and Engineering Center for Nanocarbons, Beijing National Laboratory for Molecular Sciences, College of Chemistry and Molecular Engineering, Peking University, 100871 Beijing, China;* orcid.org/0000-0003-3731-8859

Complete contact information is available at: https://pubs.acs.org/10.1021/acsnano.3c00022

Author Contributions

#H.H., M.-L.L., and B.X. contributed equally. H.H., B.X., and Y.W. prepared the samples. H.H., B.X., and H.W. performed the Raman measurement. M.L. performed the theoretical calculations. P.T. supervised the theoretical calculations. P.T., L.T., and J.Z. supervised over all the experiments and data collection. All authors contributed to the discussion of data and writing of manuscript.

Notes

The authors declare no competing financial interest.

ACKNOWLEDGMENTS

This work was financially supported by the Ministry of Science and Technology of China (2018YFA0703502, 2016YFA0200104), the National Natural Science Foundation of China (Grant Nos. 52021006, 51720105003, 21790052, 21974004, 52031014, 12004377, 11874350 and 12127807), the Strategic Priority Research Program of CAS (XDB36030100), CAS Key Research Program of Frontier Sciences (Grant No. ZDBS-LY-SLH004 and XDPB22), CAS Project for Young Scientists in Basic Research (YSBR-026) and the Beijing National Laboratory for Molecular Sciences (BNLMS-CXTD-202001). M.-L.L. also acknowledges the support from Youth Innovation Promotion Association, Chinese Academy of Sciences (No. 2023125)

REFERENCES

(1) Britnell, L.; Ribeiro, R. M.; Eckmann, A.; Jalil, R.; Belle, B. D.; Mishchenko, A.; Kim, Y.-J.; Gorbachev, R. V.; Georgiou, T.; Morozov, S. V.; Grigorenko, A. N.; Geim, A. K.; Casiraghi, C.; Neto, A. H. C.;

Novoselov, K. S. Strong Light-Matter Interactions in Heterostructures of Atomically Thin Films. *Science* **2013**, *340*, 1311−1314.
(2) Withers, F.; Del Pozo-Zamudio, O.; Mishchenko, A.; Rooney, A. P.; Gholinia, A.; Watanabe, K.; Taniguchi, T.; Haigh, S. J.; Geim, A. K.; Tartakovskii, A. I.; Novoselov, K. S. Light-Emitting Diodes by Band-Structure Engineering in van der Waals Heterostructures. *Nat. Mater.* **2015**, *14*, 301−306.
(3) Dean, C. R.; Wang, L.; Maher, P.; Forsythe, C.; Ghahari, F.; Gao, Y.; Katoch, J.; Ishigami, M.; Moon, P.; Koshino, M.; Taniguchi, T.; Watanabe, K.; Shepard, K. L.; Hone, J.; Kim, P. Hofstadter's Butterfly and the Fractal Quantum Hall Effect in Moire Superlattices. *Nature* **2013**, *497*, 598−602.
(4) Chen, G. R.; Sharpe, A. L.; Gallagher, P.; Rosen, I. T.; Fox, E. J.; Jiang, L. L.; Lyu, B. S.; Li, H. Y.; Watanabe, K.; Taniguchi, T.; Jung, J.; Shi, Z. W.; Goldhaber-Gordon, D.; Zhang, Y. B.; Wang, F. Signatures of Tunable Superconductivity in a Trilayer Graphene Moiré Superlattice. *Nature* **2019**, *572*, 215−219.
(5) Zhong, D.; Seyler, K. L.; Linpeng, X. Y.; Wilson, N. P.; Taniguchi, T.; Watanabe, K.; McGuire, M. A.; Fu, K. M. C.; Xiao, D.; Yao, W.; Xu, X. D. Layer-Resolved Magnetic Proximity Effect in van der Waals Heterostructures. *Nat. Nanotechnol.* **2020**, *15*, 187−191.
(6) Tang, C. L.; Zhang, Z. W.; Lai, S.; Tan, Q. H.; Gao, W. B. Magnetic Proximity Effect in Graphene/$CrBr_3$ van der Waals Heterostructures. *Adv. Mater.* **2020**, *32*, 1908498.
(7) Hunt, B.; Sanchez-Yamagishi, J. D.; Young, A. F.; Yankowitz, M.; LeRoy, B. J.; Watanabe, K.; Taniguchi, T.; Moon, P.; Koshino, M.; Jarillo-Herrero, P.; Ashoori, R. C. Massive Dirac Fermions and Hofstadter Butterfly in a van der Waals Heterostructure. *Science* **2013**, *340*, 1427−1430.
(8) Chen, G. R.; Sharpe, A. L.; Fox, E. J.; Zhang, Y. H.; Wang, S. X.; Jiang, L. L.; Lyu, B.; Li, H. Y.; Watanabe, K. J.; Taniguchi, T.; Shi, Z. W.; Senthil, T.; Goldhaber-Gordon, D.; Zhang, Y. B.; Wang, F. Tunable Correlated Chern Insulator and Ferromagnetism in a Moiré Superlattice. *Nature* **2020**, *579*, 56−61.
(9) Arora, H. S.; Polski, R.; Zhang, Y. R.; Thomson, A.; Choi, Y.; Kim, H.; Lin, Z.; Wilson, I. Z.; Xu, X. D.; Chu, J. H.; Watanabe, K.; Taniguchi, T.; Alicea, J.; Nadj-Perge, S. Superconductivity in Metallic Twisted Bilayer Graphene Stabilized by WSe_2. *Nature* **2020**, *583*, 379−384.
(10) Yang, J. X.; Chen, G. R.; Han, T. Y.; Zhang, Q. H.; Zhang, Y. H.; Jiang, L. L.; Lyu, B.; Li, H. Y.; Watanabe, K.; Taniguchi, T.; Shi, Z. W.; Senthil, T.; Zhang, Y. B.; Wang, F.; Ju, L. Spectroscopy Signatures of Electron Correlations in a Trilayer Graphene/hBN Moire Superlattice. *Science* **2022**, *375*, 1295−1299.
(11) Britnell, L.; Gorbachev, R. V.; Jalil, R.; Belle, B. D.; Schedin, F.; Mishchenko, A.; Georgiou, T.; Katsnelson, M. I.; Eaves, L.; Morozov, S. V.; Peres, N. M. R.; Leist, J.; Geim, A. K.; Novoselov, K. S.; Ponomarenko, L. A. Field-Effect Tunneling Transistor Based on Vertical Graphene Heterostructures. *Science* **2012**, *335*, 947−950.
(12) Georgiou, T.; Jalil, R.; Belle, B. D.; Britnell, L.; Gorbachev, R. V.; Morozov, S. V.; Kim, Y. J.; Gholinia, A.; Haigh, S. J.; Makarovsky, O.; Eaves, L.; Ponomarenko, L. A.; Geim, A. K.; Novoselov, K. S.; Mishchenko, A. Vertical Field-Effect Transistor Based on Graphene-WS_2 Heterostructures for Flexible and Transparent Electronics. *Nat. Nanotechnol.* **2013**, *8*, 100−103.
(13) Kim, Y.; Cruz, S. S.; Lee, K.; Alawode, B. O.; Choi, C.; Song, Y.; Johnson, J. M.; Heidelberger, C.; Kong, W.; Choi, S.; Qiao, K.; Almansouri, I.; Fitzgerald, E. A.; Kong, J.; Kolpak, A. M.; Hwang, J.; Kim, J. Remote Epitaxy through Graphene Enables Two-Dimensional Material-Based Layer Transfer. *Nature* **2017**, *544*, 340−343.
(14) Kim, H.; Chang, C. S.; Lee, S.; Jiang, J.; Jeong, J.; Park, M.; Meng, Y.; Ji, J.; Kwon, Y.; Sun, X.; Kong, W.; Kum, H. S.; Bae, S.-H.; Lee, K.; Hong, Y. J.; Shi, J.; Kim, J. Remote Epitaxy. *Nat. Rev. Methods Primers* **2022**, *2*, 40.
(15) Das, S.; Sebastian, A.; Pop, E.; McClellan, C. J.; Franklin, A. D.; Grasser, T.; Knobloch, T.; Illarionov, Y.; Penumatcha, A. V.; Appenzeller, J.; Chen, Z. H.; Zhu, W. J.; Asselberghs, I.; Li, L. J.; Avci, U. E.; Bhat, N.; Anthopoulos, T. D.; Singh, R. Transistors Based on Two-Dimensional Materials for Future Integrated Circuits. *Nat. Electron.* **2021**, *4*, 786−799.
(16) Zhu, K. C.; Wen, C.; Aljarb, A. A.; Xue, F.; Xu, X. M.; Tung, V.; Zhang, X. X.; Alshareef, H. N.; Lanza, M. The Development of Integrated Circuits Based on Two-Dimensional Materials. *Nat. Electron.* **2021**, *4*, 775−785.
(17) Tan, P. H.; Han, W. P.; Zhao, W. J.; Wu, Z. H.; Chang, K.; Wang, H.; Wang, Y. F.; Bonini, N.; Marzari, N.; Pugno, N.; Savini, G.; Lombardo, A.; Ferrari, A. C. The Shear Mode of Multilayer Graphene. *Nat. Mater.* **2012**, *11*, 294−300.
(18) Liang, L. B.; Zhang, J.; Sumpter, B. G.; Tan, Q. H.; Tan, P. H.; Meunier, V. Low-Frequency Shear and Layer-Breathing Modes in Raman Scattering of Two-Dimensional Materials. *ACS Nano* **2017**, *11*, 11777−11802.
(19) Quan, J. M.; Linhart, L.; Lin, M. L.; Lee, D.; Zhu, J. H.; Wang, C. Y.; Hsu, W. T.; Choi, J.; Embley, J.; Young, C.; Taniguchi, T.; Watanabe, K.; Shih, C. K.; Lai, K.; MacDonald, A. H.; Tan, P. H.; Libisch, F.; Li, X. Q. Phonon Renormalization in Reconstructed MoS_2 Moire Superlattices. *Nat. Mater.* **2021**, *20*, 1167−1167.
(20) Michel, K. H.; Verberck, B. Theory of Rigid-Plane Phonon Modes in Layered Crystals. *Phys. Rev. B* **2012**, *85*, No. 094303.
(21) Zeng, H. L.; Zhu, B. R.; Liu, K.; Fan, J. H.; Cui, X. D.; Zhang, Q. M. Low-Frequency Raman Modes and Electronic Excitations in Atomically Thin MoS_2 Films. *Phys. Rev. B* **2012**, *86*, No. 241301(R).
(22) Li, H.; Wu, J. B.; Ran, F. R.; Lin, M. L.; Liu, X. L.; Zhao, Y. Y.; Lu, X.; Xiong, Q. H.; Zhang, J.; Huang, W.; Zhang, H.; Tan, P. H. Interfacial Interactions in van der Waals Heterostructures of MoS_2 and Graphene. *ACS Nano* **2017**, *11*, 11714−11723.
(23) Wu, J. B.; Hu, Z. X.; Zhang, X.; Han, W. P.; Lu, Y.; Shi, W.; Qiao, X. F.; Ijias, M.; Milana, S.; Ji, W.; Ferrari, A. C.; Tan, P. H. Interface Coupling in Twisted Multilayer Graphene by Resonant Raman Spectroscopy of Layer Breathing Modes. *ACS Nano* **2015**, *9*, 7440−7449.
(24) Lin, M. L.; Zhou, Y.; Wu, J. B.; Cong, X.; Liu, X. L.; Zhang, J.; Li, H.; Yao, W.; Tan, P. H. Cross-Dimensional Electron-Phonon Coupling in van der Waals Heterostructures. *Nat. Commun.* **2019**, *10*, 2419.
(25) Wu, H.; Lin, M. L.; Leng, Y. C.; Chen, X.; Zhou, Y.; Zhang, J.; Tan, P. H. Probing the Interfacial Coupling in Ternary van der Waals Heterostructures. *npj 2D Mater. Appl.* **2022**, *6*, 87.
(26) Kim, K.; Coh, S.; Tan, L. Z.; Regan, W.; Yuk, J. M.; Chatterjee, E.; Crommie, M. F.; Cohen, M. L.; Louie, S. G.; Zettl, A. Raman Spectroscopy Study of Rotated Double-Layer Graphene: Misorientation-Angle Dependence of Electronic Structure. *Phys. Rev. Lett.* **2012**, *108*, 246103.
(27) Eliel, G. S. N.; Moutinho, M. V. O.; Gadelha, A. C.; Righi, A.; Campos, L. C.; Ribeiro, H. B.; Chiu, P. W.; Watanabe, K.; Taniguchi, T.; Puech, P.; Paillet, M.; Michel, T.; Venezuela, P.; Pimenta, M. A. Intralayer and Interlayer Electron-Phonon Interactions in Twisted Graphene Heterostructures. *Nat. Commun.* **2018**, *9*, 1221.
(28) Xu, B.; Hao, H.; Huang, J. Q.; Zhao, Y.; Yang, T.; Zhang, J.; Tong, L. M. Twist-Induced New Phonon Scattering Pathways in Bilayer Graphene Probed by Helicity-Resolved Raman Spectroscopy. *J. Phys. Chem. C* **2022**, *126*, 10487−10493.
(29) He, R.; Chung, T. F.; Delaney, C.; Keiser, C.; Jauregui, L. A.; Shand, P. M.; Chancey, C. C.; Wang, Y. N.; Bao, J. M.; Chen, Y. P. Observation of Low Energy Raman Modes in Twisted Bilayer Graphene. *Nano Lett.* **2013**, *13*, 3594−3601.
(30) Carozo, V.; Almeida, C. M.; Ferreira, E. H. M.; Cancado, L. G.; Achete, C. A.; Jorio, A. Raman Signature of Graphene Superlattices. *Nano Lett.* **2011**, *11*, 4527−4534.
(31) Xue, J. M.; Sanchez-Yamagishi, J.; Bulmash, D.; Jacquod, P.; Deshpande, A.; Watanabe, K.; Taniguchi, T.; Jarillo-Herrero, P.; Leroy, B. J. Scanning Tunnelling Microscopy and Spectroscopy of Ultra-Flat Graphene on Hexagonal Boron Nitride. *Nat. Mater.* **2011**, *10*, 282−285.
(32) Moutinho, M. V. O.; Eliel, G. S. N.; Righi, A.; Gontijo, R. N.; Paillet, M.; Michel, T.; Chiu, P. W.; Venezuela, P.; Pimenta, M. A. Resonance Raman Enhancement by the Intralayer and Interlayer

https://doi.org/10.1021/acsnano.3c00022
ACS Nano 2023, 17, 10142−10151

Electron-Phonon Processes in Twisted Bilayer Graphene. *Sci. Rep.* **2021**, *11*, 17206.
(33) Campos-Delgado, J.; Cancado, L. G.; Achete, C. A.; Jorio, A.; Raskin, J. P. Raman Scattering Study of the Phonon Dispersion in Twisted Bilayer Graphene. *Nano Res.* **2013**, *6*, 269−274.
(34) Zhang, X.; Han, W. P.; Wu, J. B.; Milana, S.; Lu, Y.; Li, Q. Q.; Ferrari, A. C.; Tan, P. H. Raman Spectroscopy of Shear and Layer Breathing Modes in Multilayer MoS_2. *Phys. Rev. B* **2013**, *87*, 115413.
(35) Liang, L. B.; Puretzky, A. A.; Sumpter, B. G.; Meunier, V. Interlayer Bond Polarizability Model for Stacking-Dependent Low-Frequency Raman Scattering in Layered Materials. *Nanoscale* **2017**, *9*, 15340−15355.
(36) Sun, L. Z.; Wang, Z. H.; Wang, Y. C.; Zhao, L.; Li, Y. L.; Chen, B. H.; Huang, S. H.; Zhang, S. S.; Wang, W. D.; Pei, D.; Fang, H. W.; Zhong, S.; Liu, H. Y.; Zhang, J. C.; Tong, L. M.; Chen, Y. L.; Li, Z. Y.; Rummeli, M. H.; Novoselov, K. S.; Peng, H. L.; Lin, L.; Liu, Z. F. Hetero-Site Nucleation for Growing Twisted Bilayer Graphene with a Wide Range of Twist Angles. *Nat. Commun.* **2021**, *12*, 2391.
(37) Li, X. L.; Han, W. P.; Wu, J. B.; Qiao, X. F.; Zhang, J.; Tan, P. H. Layer-Number Dependent Optical Properties of 2D Materials and Their Application for Thickness Determination. *Adv. Funct. Mater.* **2017**, *27*, 1604468.

https://doi.org/10.1021/acsnano.3c00022
ACS Nano 2023, 17, 10142−10151